

Effect of molecular hydrogen self-shielding modeling on galaxy formation in cosmological simulation

THỊNH HỮU NGUYỄN^{1,2} AND KIRK S. S. BARROW¹

¹*Department of Astronomy, University of Illinois at Urbana-Champaign, Urbana, IL 61801, USA*

²*Center for AstroPhysical Surveys, National Center for Supercomputing Applications
Urbana, IL 61801, USA*

ABSTRACT

Modeling molecular hydrogen accurately is an important task in cosmological simulation because it affects star formation and galaxy evolution. Given the increasing capabilities of computational power in recent years, more robust and computationally-heavy techniques are now achievable. One of which is the use of ray tracing to model molecular hydrogen self-shielding. This paper evaluates the use of Sobolev-like approximation in self-shielding modeling - a method widely used to reduce computational cost in literature - and test whether it agrees with the results from a more vigorous ray tracing method. We run two high resolution zoom-in cosmological simulations with two models up to redshift of 10.9 to investigate their effects of galaxy evolution in the early universe. We find that the approximation model underestimates the level of H_2 self-shielding in low gas density environment, causing halos to lose a lot of H_2 when compared with the ray tracing model. The susceptibility of H_2 against high-energy radiation in the simulation with the approximation model prevents smaller halos from forming stars, while bigger halos seem to be uninfluenced by the choice of self-shielding model in terms of stellar mass. Within a halo, we show that the discrepancy between the approximation and the ray-tracing model is more prominent in the halo's outer region due to its low gas density. On a large scale, the approximation model have fewer metal-contaminated regions in the intergalactic medium, heats up the universe quicker, and speeds up the reionization process. These results show that the Sobolev-like approximation to model H_2 self-shielding alter various properties of galaxies and the large-scale universe, emphasizing a need for caution when employing this technique in running cosmological simulations.

Keywords: Astronomical simulations(1857) — Radiative transfer simulations(1967) — Galaxy formation(595) — Reionization(1383)

1. INTRODUCTION

Molecular hydrogen is a building block for star formation. For a gas cloud to collapse into a star, the cloud's self-gravity must be sufficiently large to overcome its pressure gradient. In the absence of other environmental effects, to achieve the collapse, the gas cloud usually needs to have sufficient mass or a high enough cooling rate so that the cooling time is smaller than the free-fall time. Since the cooling time generally decreases when the gas density increases during the collapse, this leads to catastrophic cooling and the gas pressure being lost against gravity, resulting in a collapse. Depending on the temperature and density, there are multiple radiative cooling mechanisms for a cloud to release its internal energy. For primordial gas clouds with atomic hydrogen HI being the dominant component, Bremsstrahlung

⁴³ emission, atomic hydrogen's recombination, collisional ionization, and collisional excitation processes can help cool the gas down to at best the virial temperature of ⁴⁶ $10^4 K$, below which the cooling rate is too low ([Thoul & Weinberg 1995](#)). However, if molecular hydrogen H_2 is available or is created from atomic hydrogen, it can further stimulate cooling by opening up new cooling channels through its rotational and vibrational energy levels. ⁵¹ This allows the gas to cool to ≈ 100 Kelvin degrees ([Galli & Palla 1998](#)), making it possible for the cloud to collapse into stars. This connection between star formation and H_2 can be reflected through the Kennicutt-Schmidt law ([Schmidt 1959; Kennicutt 1998](#)) and various observational evidence in nearby disk galaxies ([Wong & Blitz 2002; Kennicutt et al. 2007; Leroy et al. 2013](#)). ⁵⁷ Ultraviolet (UV) radiation emitted by nearby active stars can photodissociate molecular hydrogen via the

⁶⁰ Solomon process (Solomon 1965 - private communication reported in Field et al. 1966, Stecher & Williams
⁶¹ 1967). When absorbing a Lyman-Werner (LW) photon
⁶² (11.2-13.6 eV), a molecular hydrogen molecule is
⁶³ excited from the ground state to an excited electronic
⁶⁴ state. Instead of radiatively decaying back to the bound
⁶⁵ state, about 15 percent of the molecules have their elec-
⁶⁶ trons decay into the vibrational continuum, which sub-
⁶⁷ sequently dissociates the molecule into atomic hydrogen.
⁶⁸ Dissociation rates through this mechanism can be in-
⁶⁹ hibited through H_2 self-shielding, a phenomenon where
⁷⁰ the column density is large enough that the H_2 in the
⁷¹ cloud's outer layer absorbs the LW radiation and hence
⁷² shields the inner region. Previous studies point out the
⁷³ importance of including self-shielding in preserving the
⁷⁴ amount of molecular hydrogen required for star forma-
⁷⁵ tion. When simulating a disc galaxy, (Christensen et al.
⁷⁶ 2012) notices an increase in the amount of cold gas and
⁷⁷ a clumpier interstellar medium when incorporating self-
⁷⁸ shielding in their simulation. Safranek-Shrader et al.
⁷⁹ (2017) finds that self-shielding is crucial in the devel-
⁸⁰ opment of H_2 in the disc's mid-plane, which accounts
⁸¹ for 10-15 percent of the total gas mass. Therefore, the
⁸² hydrogen self-shielding mechanism becomes pivotal in
⁸³ preserving the amount of molecular hydrogen and regu-
⁸⁴ lating star formation.

⁸⁵ Through modeling a semi-infinite, static slab of gas
⁸⁶ irradiated on one surface, Draine & Bertoldi (1996) pro-
⁸⁷ poses an analytical expression to model H_2 self-shielding
⁸⁸ factor that includes the effect of **line overlap (do we**
⁸⁹ **need to elaborate this? also do we need to show**
⁹⁰ **the equation here)**. Maybe show all the papers
⁹¹ **that use this expression? Look at Hartwig+2015**
⁹² **for the list** As shown in Equation (37) of Draine
⁹³ & Bertoldi (1996), the self-shielding factor is a func-
⁹⁴ tion of the H_2 column density. In the past, comput-
⁹⁵ ing the column density for multiple 3D directions was
⁹⁶ prohibitively computationally expensive (Shang et al.
⁹⁷ 2010; Wolcott-Green et al. 2011). Therefore, multi-
⁹⁸ ple methods have been suggested to approximate the
⁹⁹ self-shielding effect while trying to alleviate its demand-
¹⁰⁰ ing computational cost. A method is to define a lo-
¹⁰¹ cal characteristic length scale across which the H_2 num-
¹⁰² ber density is constant. This characteristic length can
¹⁰³ be either the Jeans length (Shang et al. 2010; Johnson
¹⁰⁴ et al. 2011), the Sobolev length (Sobolev 1957; Yoshida
¹⁰⁵ et al. 2006), or the Sobolev-like length that is computed
¹⁰⁶ from the density-gradient (Gnedin et al. 2009; Gnedin
¹⁰⁷ & Kravtsov 2011). Rather than a single characteris-
¹⁰⁸ tic length, Hartwig et al. (2015a) approximates the 3D
¹⁰⁹ column densities by creating spherical maps of the col-
¹¹⁰ umn density around each Voronoi cell with 48 equal-area

¹¹² pixels and also taking into account the Doppler effect
¹¹³ from the relative velocities of the infalling gas particles.

¹¹⁴ Another non-local method is the six-ray approximation
¹¹⁵ (Yoshida et al. 2003, 2007; Glover & Mac Low 2007a,b),
¹¹⁶ where the H_2 column density is integrated along six
¹¹⁷ directions along three Cartesian axes centered at each
¹¹⁸ particle's position. Many cosmological simulations use
¹¹⁹ one of these approximations to reduce the computational
¹²⁰ costs, for example, the Christensen et al. 2012's simula-
¹²¹ tion, the COLDSPIM simulation (Maio et al. 2022), and
¹²² the Renaissance Simulations (O'Shea et al. 2015).

¹²³ However, there are limitations to the applicability of
¹²⁴ approximate treatments in various test problems when
¹²⁵ compared to the accurate full ray-tracing calculation. In
¹²⁶ the context of photodissociation of H_2 in protogalaxies
¹²⁷ and direct-collapse black hole formation, Wolcott-Green
¹²⁸ et al. (2011) show that the Sobolev length, the density
¹²⁹ gradient, and the six-ray approximation methods over-
¹³⁰ estimate the H_2 shielding degree by an order of mag-
¹³¹ nitude in low-density regions of $n < 10^4 \text{ cm}^{-3}$. Also
¹³² in the context of direct-collapse black hole, when com-
¹³³ paring with their non-local approximation detailed in
¹³⁴ Hartwig et al. (2015a), Hartwig et al. (2015b) find that
¹³⁵ the Jeans approach returns a critical flux value J_{crit} -
¹³⁶ the lowest flux required for a halo with virial temper-
¹³⁷ ature above 10^4 K to collapse to a supermassive black
¹³⁸ hole seed - two times larger than the non-local approx-
¹³⁹ imation, leading to a disparity in the predicted number
¹⁴⁰ density of black hole seeds. Greif (2014) investigate the
¹⁴¹ collapse of primordial star-forming clouds with an accu-
¹⁴² rate H_2 line emission model and notice that the Sobolev
¹⁴³ method brings about a thermal instability for the col-
¹⁴⁴ lapsing cloud and an order-of-magnitude overestimation
¹⁴⁵ of the escape fraction for high optical depth. When eval-
¹⁴⁶ uating the triggered Population III star formation at the
¹⁴⁷ limb of the HII region, Chiaki & Wise (2023) find that
¹⁴⁸ while the density-gradient method matches well with the
¹⁴⁹ ray-tracing method, the Jeans length approximation re-
¹⁵⁰sults in an overestimation of the number of the Pop-
¹⁵¹ulation III stars at the front of the shock wave. The
¹⁵² authors suggest that this is because the thickness of the
¹⁵³ H_2 ring of the shock front is typically smaller than the
¹⁵⁴ Jeans length, and thus the local approximation is inap-
¹⁵⁵propriate. In their large-scale galactic discs simulations,
¹⁵⁶ Safranek-Shrader et al. (2017) notices that the Sobolev
¹⁵⁷ method underpredicts the H_2 abundance in the disc by
¹⁵⁸ a factor of 5, while the six-ray and the Jeans length
¹⁵⁹ methods perform better, which is contrary to the find-
¹⁶⁰ings that Jeans length method is ineffective in previ-
¹⁶¹ous studies. Thus, the validity of these approximation
¹⁶² methods is highly problem-dependent and they cannot

be used as a general substitution for the full ray-tracing calculation.

In this paper, we expand the investigation by comparing the Sobolev-like density-gradient approximation model (Gnedin et al. 2009) with the detailed ray-tracing methods in the context of star formation during the Reionization period. This will help further examine and inform the community about the applicability of these approximations in modeling H_2 in different contexts. In Section 2, we will describe our simulation, the implemented H_2 self-shielding models, and our methodology for analysis. Section 3 analyzes the effect of these models on star formation and galaxy evolution. This section will be subdivided into smaller sections that discuss the effect of self-shielding model on individual galaxies and on the large scale universe. Last but not least, in Section 4, we discuss the implications of the findings and summarize the paper.

181

2. METHOD

2.1. Comoslogical simulations

We run and analyze outputs from a radiation-hydrodynamic adaptive mesh refinement simulation ENZO (Bryan et al. 2014). Two sets of cosmological simulations are generated to explore the self-shielding effect in the early stage and in the late stage of the Reionization period, which we will refer to as *EarlyRe* and *LateRe*, respectively. In the early stage of Reionization, the UV background radiation is still local. Thus, the *EarlyRe* set provides a control sample to study whether the self-shielding approximation affects the overall star formation activity during a low non-local UV-radiation scenario. On the other hand, the *LateRe* allows us to study how the resistance of molecular clouds against a strong photoionization background depends on the self-shielding treatments. Both sets assume a flat Λ CDM cosmology and are run with the cosmological parameters obtained from Planck Collaboration et al. (2016): $\Omega_M = 0.3065$, $\Omega_\Lambda = 0.6935$, $\Omega_b = 0.0483$, $h = 0.679$, $\sigma_8 = 0.8154$, and $n = 0.9681$. The total moving volume of the *EarlyRe* and *LateRe* simulations are 13 (Mpc/h)³ and 5 (Mpc/h)³, respectively. Both sets have the root grid dimension of 256³. The total number of dark matter particles is $\approx 10^{7.82}$ particles for the *EarlyRe* set and $\approx 10^8$ particles for the *LateRe* set. Inside the total volume of the *EarlyRe* (*LateRe*) simulation, we create a smaller zoom-in region using three additional levels of nested refinement to create an effective grid size resolution of $2632.5 \times 2512.9 \times 2871.9 \text{ kpc}^3$ ($920.5 \times 1564.8 \times 1196.6 \text{ comoving kpc}^3$) at the last snapshot at redshift of 10.9 (6.4). In the zoom-in region,

the most refined dark matter particle mass is 2.7×10^4 (1.5×10^3) M_\odot . As the density passes a certain threshold, the grids inside this zoom-in region can further be refined adaptively up to 2^{13} (2^{14}) times the root grid dimensions. This allows a maximum spatial resolution down to 3.07 pc (1.89 pc) at the last time step, which allows the tracking of large molecular clouds through initial collapse. We use radiative star cluster particle (Wise & Cen 2009) and Population III star particle (Abel et al. 2007) for our star formation prescription.

Each set contains a version running with detailed ray-tracing calculation (*EarlyRe-ray* and *LateRe-ray*) and a version running with a local approximation of the column density (*EarlyRe-apx* and *LateRe-apx*) when computing the H_2 self-shielding factor. The self-shielding model is set by the *RadiativeTransferOpticallyThinH2* ENZO radiation parameter, where a value of 1 enables an optically thin H_2 dissociating Lyman-Werner radiation field and a value of 0 uses ray-tracing for the calculation. For the *EarlyRe* simulation set, the *EarlyRe-ray* and the *EarlyRe-apx* are initialized with an identical list of parameters and initial conditions except for the *RadiativeTransferOpticallyThinH2* parameter. We evolve the two simulations from $z = 100$ to $z \approx 10.9$, each output is 1 Myr apart. For the *LateRe* set, to save computational time, we run the two simulations without ray-tracing until $z \approx 7.3$, then we switch the *RadiativeTransferOpticallyThinH2* parameter to 0 for one of the simulations (the *LateRe-ray*) and run both of them until $z \approx 6.4$. This allows us to examine the effect of self-shielding near the end of the reionization epoch.

2.2. Halo tracking and merger tree algorithms

To identify the halos in the simulations, we employ SHINBAD (Barrow et al 2025, in preparation), an all-in-one algorithm that both finds halos and builds merger trees based on robust energy definition and particle tracking of dark matter particles. (A few more sentences about SHINBAD by Kirks). We exclude all the halos that are outside the refined region of the simulation box - the region containing only the highest and the second-most highest resolution dark matter particles - to ensure that the halos are physical.

2.3. Numerical H_2 self-shielding models

A H_2 self-shielding process happens when a molecular cloud has a sufficiently high column density that its outer layer absorbs all the Lyman-Werner UV photons, effectively shielding the molecules within it against photodissociation. Via modeling a semi-infinite, static slab of gas that is irradiated on one surface, Draine & Bertoldi (1996) express a self-shielding-accounted pho-

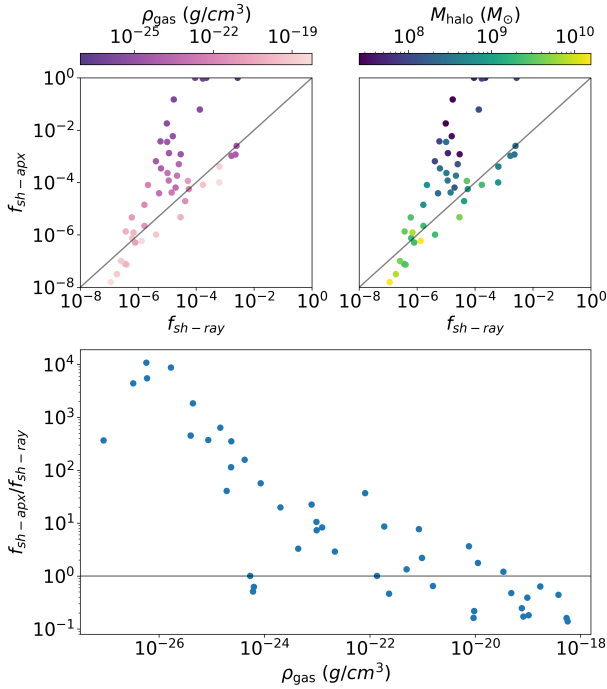


Figure 1. The comparison between the self-shielding factor between the *EarlyRe-ray* and the *EarlyRe-apx* simulation, evaluated at $z = 10.9$. Two gas cells with the highest gas density and highest gas density gradients are chosen in 31 halos in different mass range to evaluate the self-shielding factors. (Top) The relationship between the self-shielding factors calculated by the Sobolev-like approximation model and the ray-tracing model, colored by the cell's gas density (top left) and the host halo's mass (top right). (Bottom) The ratio between the approximated and the ray-traced self-shielding factors is plotted as a function of gas density. The Sobolev-like approximation tends to overestimate the amount of H_2 self-shielding in the high gas density regime and underestimate it in the low gas density regime.

264 to dissociation rate as

$$265 \quad k_{\text{diss}}(N_{H_2}, T) = f_{sh}(N_{H_2}, T) \cdot k_{\text{diss}}(N_{H_2} = 0, T), \quad (1)$$

266 where $f_{sh}(N_{H_2}, T)$ is a self-shielding factor or shield-
267 ing function, and $k_{\text{diss}}(N_{H_2} = 0, T)$ is the dissociation
268 rate in a optically-thin regime. At a low temperature
269 (hundreds of K), the self-shielding factor can be approx-
270 imately computed from only the H_2 column density,

$$271 \quad f_{sh} = \min \left[1, \left(\frac{N_{H_2}}{10^{14} \text{cm}^{-2}} \right)^{-3/4} \right]. \quad (2)$$

272 This is controlled by setting the ENZO radiation pa-
273 rameter `RadiativeTransferH2ShieldType` = 0, which
274 is also its default value. We use this expression to cal-
275 culate the self-shielding factor in the EarlyRe-apx sim-
276 ulation. It is important to note that the convention of
277 f_{sh} value is slightly counter-intuitive: the f_{sh} value of 0

278 means full self-shielding is available, and the f_{sh} value
279 of 1 means there is no self-shielding. We also acknowl-
280 edge that [Draine & Bertoldi \(1996\)](#) lists a more accurate
281 formula to calculate f_{sh} that takes temperature as a pa-
282 rameter. However, using this formula does require addi-
283 tional computational resources that we save to run the
284 ray-tracing scheme. Thus, we choose to use the approx-
285 imated expression at low temperatures. [Check Gnedin
286 and Draine 2014, where they do a comparison
287 between this equation with a more accurate one
288 \(including line overlap\).](#) Summarize their results
289 here.

290 [Maybe talking about the limitations of Draine
291 and Bertoldi 1996, as on page 5, right column of
292 Wolcott-Green.](#)

293 To avoid the high computational expense of finding
294 the H_2 column density in multiple 3D directions, previ-
295 ous studies employ different techniques to approximate
296 it (see Section 1). In this paper, we compare the results
297 from two methods: a direct integration from ray tracing
298 and a Sobolev-like length approximation ([Gnedin et al.
299 2009; Wolcott-Green et al. 2011](#)). Even though demand-
300 ing more computational time, the ray tracing treatment
301 ensures a more accurate radiative transfer calculation.
302 ENZO uses the adaptive ray tracing technique ([Wise
303 & Abel 2011](#)) that is based on the HEALPix (Hierar-
304 chical Equal Area isoLatitude Pixelation, [Gorski et al.
305 2005](#)) scheme. The column density is integrated along a
306 HEALPix rays,

$$307 \quad N_{H_2} = \int n(H_2) ds. \quad (3)$$

308 The Sobolev-like treatment is a local approximation
309 in which the number density n_{H_2} is assumed to be con-
310 stant within a characteristic length scale L_{char} . In the
311 Sobolev-like approximation, the characteristic length
312 scale is defined as a distance over which the cell's gas
313 density ρ diminishes. The gas beyond this distance is
314 sparse enough that its influence on shielding is negligi-
315 ble, and thus molecular hydrogen is dissociated in an
316 optically thin fashion. The column density is then com-
317 puted by

$$318 \quad N_{H_2} \approx n_{H_2} L_{\text{char}} = n_{H_2} \frac{\rho}{|\nabla \rho|} \quad (4)$$

319 The approximation is enabled by setting the ENZO
320 parameters `RadiativeTransferOpticallyThinH2` = 1
321 and `RadiationShield` = 2.

322 Figure 1 compares the self-shielding factor f_{sh} be-
323 tween the ray-tracing model and the Sobolev-like ap-
324 proximation model. At the time step corresponding to z
325 = 10.9, we select 31 halos that contain stars or overlap

with another halo that contains stars. For each halo, we select two gas cells to evaluate the self-shielding factor: (1) the gas cell with the highest gas density, and (2) the gas cell with the highest gas density gradient. Each scatter point in Figure 1 represents a selected gas cell. In the approximation model, the self-shielding factor of a gas cell is calculated using Equations 2 and 3. For the ray-tracing model, since the simulation output does not store the photodissociation rate calculation, we need to re-compute the self-shielding factor using Equation 2 with an attenuated LW flux-weighted average column density. The LW flux from each star to a selected gas cell is calculated as follows. Firstly, the intrinsic spectrum of a star particle is generated using the Flexible Stellar Population Synthesis (fsps) with the age and metallicity of the star particle as inputs. We assume an initial mass function from Davé (2008) evaluated at $z = 0$, and we use the MIST isochrone library and MILES spectral library to generate the spectra. (may cite Susie's paper here or ask her for more information). Then, we calculate the attenuation by including both scattering and absorption due to H/He and metals (Ask Kirk to include how the absorption and scatterings are computed). With the scattering and absorption coefficients, we can compute the total optical depth and then the attenuation of the stellar spectrum from the source to the target gas cell. Lastly, we calculate the attenuated flux of each source to the gas cell, compute the LW flux-weighted average H_2 column density, and get the self-shielding factor from the ray-tracing model. It is important to note that we only include stars within the halo's virial radius to estimate the flux-weighted average H_2 density because stars outside the radius are too far from the selected gas cell to contribute considerably to the total flux at the selected gas cell.

Figure 1 demonstrates a clear disparity in the f_{sh} value between EarlyRe-apx and EarlyRe-ray. In particular, the approximation model tends to overestimate the amount of shielding for cells with a gas density larger than $10^{-20} g/cm^3$ by up to 1 dex. On the other hand, diffuse gas is subjected to underestimated H_2 self-shielding when the Sobolev-like approximation model is used. For highly diffuse gas, this underestimation can be up to 3–4 dex. This connection between gas density and f_{sh} implies a mass-dependent effect of the self-shielding approximation model on halos. The top right subfigure of Figure 1 shows that larger halos ($M_{\text{halo}} > 10^{9.5} M_\odot$) have their molecular cloud region over-shielded in the approximation model because the gas is denser. On the other hand, the molecular clouds in small halos ($M_{\text{halo}} < 10^{8.5} M_\odot$) are under-shielded against LW radiation when using the Sobolev-like approximation. In

some cases, the approximation returns no shielding effect even though those gas cells are still weakly shielded ($f_{sh} \approx 10^{-3}$ when ray-tracing is utilized). Only molecular gas clouds in halos whose mass is about $10^9 M_\odot$ are well modeled in the approximation model. The significance of this effect on star formation will be explored in Section 3.1.

(Maybe a comparison in terms of the time run between the two methods)

2.4. Cross-matching halos

To examine how each individual halo is affected by the implementation scheme of H_2 self-shielding, we perform cross-matching between halos in the simulations with ray-tracing and their counterparts in the simulations with the Sobolev-like approximation. The matching requirements are

$$\frac{2}{3} < \frac{M_{\text{vir}_{\text{ray}}}}{M_{\text{vir}_{\text{apx}}}} < \frac{3}{2}$$

$$\frac{d_{\text{COM}}}{R_{\text{vir}_{\text{ray}}}} < 0.5, \quad \frac{d_{\text{COM}}}{R_{\text{vir}_{\text{apx}}}} < 0.5 \quad (5)$$

If there are multiple halos matching to one halo, we select the pair with lowest $\frac{d_{\text{COM}}}{R_{\text{vir}}}$ value. The virial mass and radius in Equation 5 come from SHINBAD and are calculated using only dark matter. We cross-match all the halos at the last timestep of the simulations and then trace back their merger tree (details in Subsection 2.2).

2.5. Star assignment

We uniquely assign each star particle in the simulation to one dark matter halo in a two-step fashion. For the first step, a star particle is assigned to a halo where it is first created. If a star particle is created inside the intersection of multiple halos, we will calculate the orbital energy of that star particle with respect to each halo's center to determine which halo the particle belongs to. The assigned halo is the one with lower relative total orbital energy. We assume that a star particle never leaves its assigned halo unless that halo merges with another one, in which case the star particle will become a member of the descendant halo of the merger. This assumption allows a quick assignment of stars to halos without the need to calculate the orbital energy of each star to multiple halos, which is computationally expensive. The assignment's first step starts from the first snapshot to the last snapshot of the simulation.

Even though stars do not generally leave a halo's potential well for isolated halos, the behavior becomes more complex during halo-halo interaction as stripping can occur and stars can be lost from one halo to another (Kannan et al. 2015). Therefore, the second step of our

process is to address this shortcoming of the first step's assumption and to refine the star assignment result. In this step, we validate the output from the first step and check whether a star remains in its assigned halo's virial radius throughout its lifetime. If a star escapes the virial radius of its originally assigned halo, we assign that star to a new halo under two conditions: (1) the star's position must be within the new halo's virial radius and (2) the star's total orbital energy with respect to the new halo must be negative. Similar to the first step, if a star is located inside multiple potential new halos, we assign that star to the halo with the lowest negative orbital energy. If either Condition (1) or (2) fails at a certain timestep, this suggests that the star is stripped out of the potential well of all halos and thus we remove that star from the halo assignment process of that time step.

Once each star particle is uniquely associated with one halo, we calculate a halo's stellar mass and SFR exclusively based on its member star particles. This gravitational unbinding of star particles guarantees that each halo's stellar mass profile are not overlap and independent of each other.

2.6. Defining ISM, CGM, and IGM

The boundary of the interstellar medium (ISM), the circumgalactic medium (CGM), and the intergalactic medium (IGM) region in our analysis is defined as follows. The ISM region (or the boundary of a galaxy) starts from the galaxy's center of mass to $R_{\text{bary},2000}$, which is the radius enclosing a baryonic (gas and stars) mass density 2000 times the universe's critical mass density at a certain redshift. Even though there are multiple other definition of the boundary of galaxy in literature, such as using a fixed fraction of the virial radius, a fixed physical radius, or a radius that is scaled with mass or surface brightness (see Stevens et al. 2014 for a summary of these techniques), our over-density approach helps define the galaxy more robustly and more physically because it is redshift and density dependent. It also helps better define the galaxy during a close galaxy interaction when a half-mass radius or half-light radius approach may fail as another galaxy is in the target galaxy's virial radius. Depending on the redshift and the galaxy's compactness, $R_{\text{bary},2000}$ typically ranges from 0.15 to 0.25 times the halo's virial radius, which falls in the same range as other galaxy's aperture definitions in cosmological simulations (Stevens et al. 2014). The CGM starts from $R_{\text{bary},2000}$ to $R_{\text{halo,vir}}$, and the IGM is the region outside of the virial radius of all halos.

Also, it is important to note that the baryonic center of mass does not always coincide with the halo's center of mass. Thus, in some cases, we shift the virial region

to be centered on the gas and stellar mass instead of the dark matter mass; however, this shift is not large and does not affect our interpretation.

3. RESULTS

3.1. Effect on the molecular hydrogen content and star formation

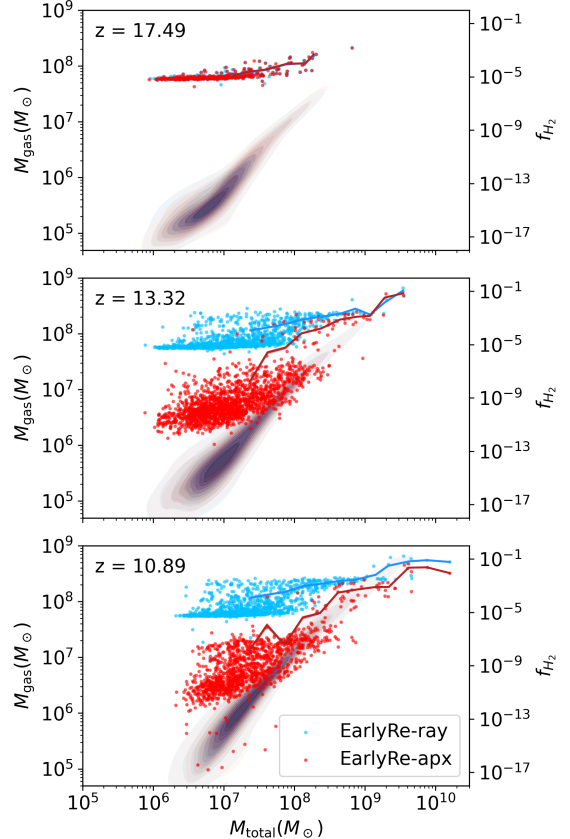


Figure 2. The relationship between the H_2 fraction and the total mass in the timestep where stars first appear, in the intermediate, and in the last timestep of the *EarlyRe* dataset. The contour plots show the M_{gas} distribution and the scatter points show the H_2 fraction of all halos in the simulation box.

Because the column density approximation model directly concerns the calculation of the molecular hydrogen density, we first investigate the amount of H_2 in the ray tracing and approximation treatment. Figure 2 shows the H_2 fraction (f_{H_2}), which is the ratio between the H_2 mass with the total gas mass, as a function of the total halo mass in three snapshots, one at the time where star particles first appear in the simulations ($z \approx 17.49$), one at the time step in the middle of the simulation run ($z \approx 13.32$), and one being the last time step of the run ($z \approx 10.9$). Each halo in the snapshot is repre-

sented by a scatter point, the line represents the running average of each total mass bin, and the shaded region around the line is the standard deviation of the scatter points within each mass bin. The contour plots represent the distribution of the halos in the $M_{\text{gas}} - M_{\text{total}}$ space. According to Figure 2, both EarlyRe-ray and Early-apx simulations have similar gas mass distribution across all timesteps, showing f_{H_2} represents the amount of H_2 in the halos. However, f_{H_2} shows a notable difference between the two radiative transfer treatments, especially at the later time step and in the lower-halo-mass regime. For halo mass smaller than $10^8 M_\odot$, the f_{H_2} in the ray-tracing treatment is larger than that of the Sobolev-like approximation treatment by 3 to 6 dex. This difference grows larger as the simulation evolves, reaching up to 12 dex at the last time step for small halos. The EarlyRe-ray simulation also develops a lower limit for f_{H_2} of around 10^{-5} , whereas the f_{H_2} is allowed to reach much further value in the EarlyRe-apx simulation. This shows that the ray-tracing treatment models the self-shielding effect much better and thus helps preserve more molecular hydrogen in the halos. As pointed out in Figure 1, the approximation treatment considerably underestimates H_2 self-shielding in a low gas density regime and molecular hydrogen to get photodissociated more easily, inferring that smaller halos are the most susceptible to the choice of the model. At a higher mass range, the difference in f_{H_2} between the two models gradually diminishes. This is reasonable because larger halos have deeper gravitational potential well and have more dense cool gas regions where H_2 exists. In these regions, the approximation model matches well with the ray-tracing model (as shown in Figure 1), leading to an agreement of f_{H_2} between the two runs.

We proceed to investigate whether the self-shielding treatment affects the stellar mass of galaxies in the simulation. Figure 3 shows the relationship between stellar mass and halo mass between the *Early-Ray* and *Early-apx* in the time step where stars first appear (top left panel), in the last time step of the dataset (bottom right panel), and in the intermediate time steps. Figure 4 displays the number of halos that host stars as a function of time for different halo mass bins. The stellar component of the halos is unbound by using the star assignment procedure described in Section 2.5. Even though the number of halos with stars is even between *EarlyRe-apx* and *EarlyRe-ray* in the beginning, there are more halos with stars in *EarlyRe-ray* at the end of the simulation, particularly halos with $M_{\text{halo}} < 10^9 M_\odot$. For ease of reference and lack of a better term, we will use the term "galaxy" to refer to a halo with stars, as opposed with halos with only gas and dark matter parti-

cles. From 375 million years after the Big Bang to near the end of the simulation ($z \approx 11.88 - 11$), there are two to four galaxies more in the simulation with the ray-tracing treatment. Furthermore, at a similar halo mass, smaller halos in *EarlyRe-ray* tend to have more stars than their counterparts in *EarlyRe-ray* by several dex in solar mass. This indicates that the use of Sobolev-like approximation for H_2 self-shielding treatment inhibits star formation activity in small halos and dwarf galaxies. On the other hand, halos whose dark matter mass is larger than $10^9 M_\odot$ show good agreement in stellar mass, suggesting that the stellar components of large halos are unaffected by our choice of H_2 self-shielding model. This observation aligns with Figure 2, where we see that H_2 is more accurately shielded in higher halo mass in *EarlyRe-apx*.

Even though we show that stars form easier in smaller halos when using a ray-tracing model, readers may notice in Figure 4 that star particles first appear in *EarlyRe-apx* simulation rather than *EarlyRe-ray*. The formation of the first galaxy in *EarlyRe-apx* occurs 16 million years before that in *EarlyRe-ray*, and the two first galaxies both form in the same cross-matched halo whose dark matter mass is smaller than $10^9 M_\odot$ (for easier reference, we will call this halo *Halo FS*). This is quite intuitive and contrasting to our arguments. However, further investigation suggests that the timing discrepancy in the formation of first stars is likely due to the simulation's numerical stochastic nature rather than a physical reason. We examine the gas properties of *Halo FS* in both models and notice that in *EarlyRe-apx*, for cold gas region with temperature lower than 100K, there is one gas cell with a gas density of $\approx 10^{-22} \text{ g/cm}^3$, 4 dex higher than the density of surrounding cells. This gas cell is also at a higher refinement level than what we observe in the cold gas region of *EarlyRe-ray*. In our simulations, a cell is refined by two criteria: by baryon mass or by particle mass. Because the baryon mass is relatively similar between the two models, the refinement of that gas cell is likely due to a high concentration of dark matter particles. Thus, we speculate that at an earlier time step, the cell has more dark matter particles in *EarlyRe-apx* than in *EarlyRe-ray*, leading to it being subdivided. After the subdivision, the child cell increases in gas density and thus becomes more shielded. Higher self-shielding protects more H_2 and leads to more cooling, allowing gas to collapse and reach higher density in that particular gas cell, which in turn provides more shielding to H_2 according to the approximation model. This runaway effect makes this gas cell very dense and filled with H_2 , eventually leading to star formation. However, this effect happens only in a single

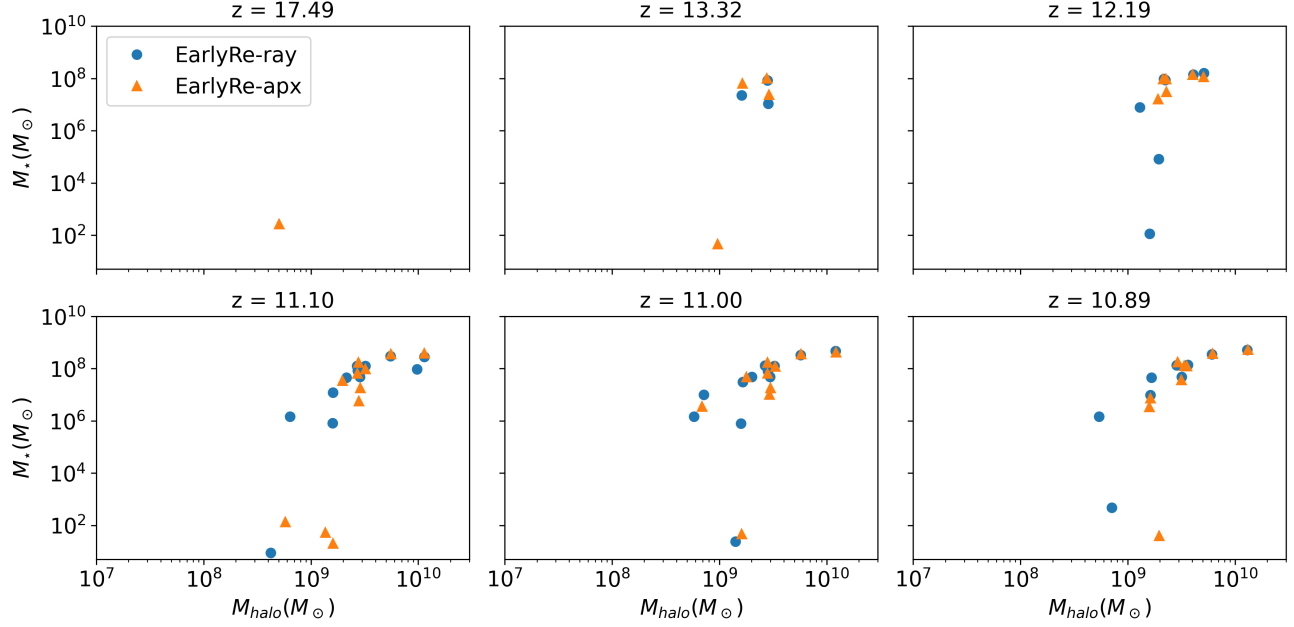


Figure 3. The relationships between stellar mass and total mass of all the halos in the timestep where stars first appear, in the intermediate timesteps, and in the last timestep of the *EarlyRe* dataset.

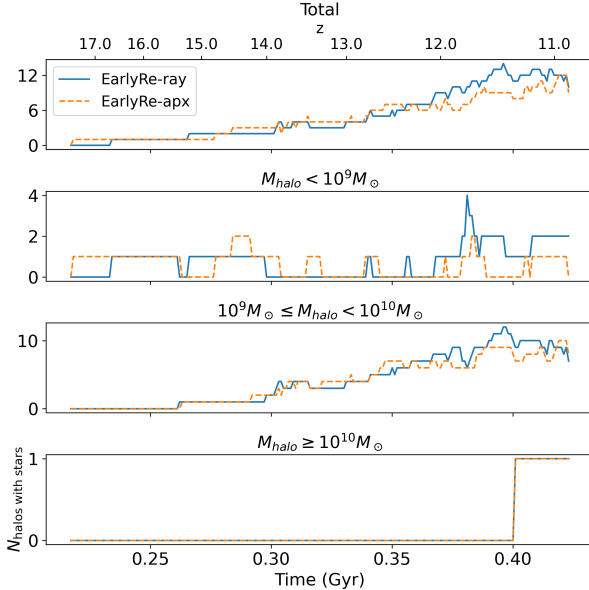


Figure 4. The comparison of the number of halos with stars as a function of time for each halo mass bin between the *EarlyRe-ray* and the *EarlyRe-apx* simulations.

gas cell and should not be considered as a global effect of the approximation model. Apart from that single cell, the average H_2 mass in the halo is still higher and the average temperature in the halo is still lower in the ray-tracing simulation, which is consistent with the general observation.

3.2. Case study on star formation

In this section, we analyze the properties of two halos, one being the largest halo in the simulation and one having a halo mass of $\approx 1.7 \times 10^9 M_\odot$, which is in the mass range where the approximation in H_2 self-shielding fails to accurately model star formation, as suggested in Figure 3. We match the halos between *EarlyRe-ray* and *EarlyRe-apx* using the procedure in Section 2.4. These two pairs of halos serve as examples to how the H_2 self-shielding modeling affects the galaxy properties.

Figures 5 and 6 show the projection of various properties at the last time step and the time evolution of those properties for the two halos in our case study. As hinted earlier by Figure 2, gas mass stays consistent between *EarlyRe-apx* and *EarlyRe-ray* throughout the halo's evolution and thus is unaffected by the choice of H_2 self-shielding modeling. The gas density projection plot also looks relatively similar between our two runs. However, even though there is an agreement on total gas content, the amount of H_2 is considerably different in two simulations. For the largest halo, the mass of H_2 starts to diverge around $z \approx 14$, and *EarlyRe-ray* has about 10 times more H_2 in that halo than *EarlyRe-apx*. For the smaller halo, the discrepancy in the H_2 content is much more severe. Early in the simulation, the ray-tracing model consistently returns about 0.5 dex more mass than the approximation model. At $z \approx 11.5$, while *EarlyRe-ray* witnesses an quick rise in molecular gas, *EarlyRe-apx* maintains the same level of H_2 , intensifying the difference to be up to 2 dex in M_{H_2} between the two simulations at the last snapshot. This difference

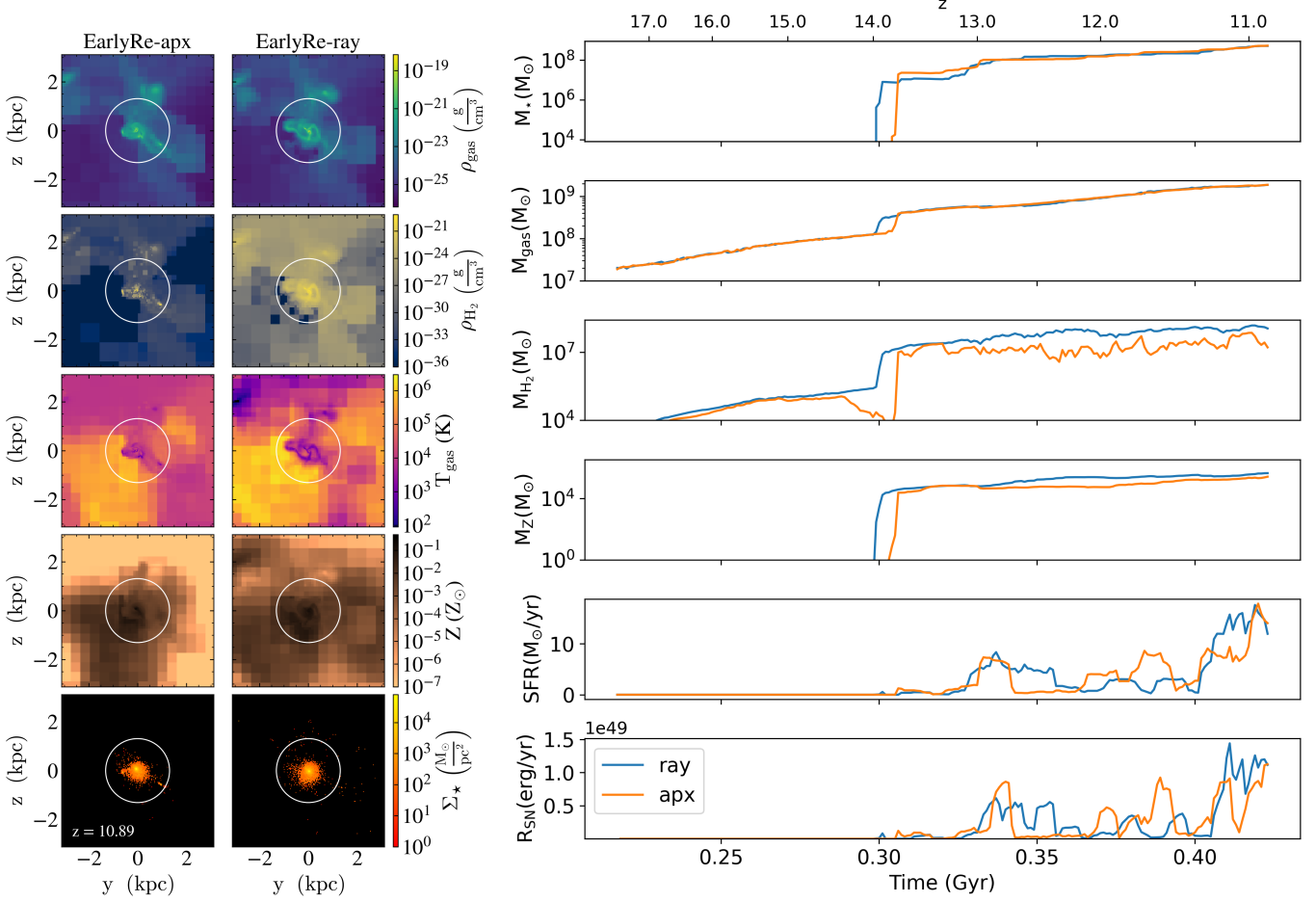


Figure 5. (Left) The gas density, H_2 density, temperature, metallicity, and stellar surface density projection plot of Halo 0 ($M_{\text{halo}} \approx 1.3 \times 10^{10} M_\odot$ at $z = 10.89$) within one virial radius. The white circle represents the boundary of the galaxy, which is defined as the radius enclosing the baryonic density 2000 times larger than the critical density of the universe. (Right) The time evolution of different properties in Halo 0 between the *EarlyRe-ray* and *EarlyRe-apx* simulations.

in H_2 matches our observation in Figure 2. In addition to H_2 mass, the distribution of molecular hydrogen is also different. In both halos that we use as examples, molecular hydrogen exists in clumps of high density ($\approx 10^{-21} \text{ g/cm}^3$) with respect to the surrounding. These clumps are located inside the galaxy (indicated by the white circle in the figures) and are concentrated in the galactic center. Outside of these clumps, H_2 gas density is quite low, reaching down to 10^{-36} g/cm^3 , proving that H_2 is completely photo-dissociated. In contrast, the halos in the *EarlyRe-ray* set displays a much more uniform distribution of molecular hydrogen. While H_2 density is still highest at the halo's center, H_2 density in the surrounding region is only 2-3 dex lower, showing that H_2 is able to exist and form in the outer part of the galaxy and even in the CGM. Indeed, the existence of H_2 outside the galactic center is what causes

the discrepancy in the H_2 fraction between *EarlyRe-apx* and *EarlyRe-ray*. More details on the topic of ISM and CGM will be discussed in Section 3.3.

With regards to stellar mass, the different in self-shielding modeling results in greater differences in smaller halos than in bigger halos, as pointed out in Figure 3. For the case of the biggest halo in the simulation, Figure 5 shows that the stellar mass of the halo converge after $z \approx 13$, even though *EarlyRe-ray* forms its first stellar particles a few million years earlier. On the other hand, for the smaller halo in Figure 6, the halo modeled with ray-tracing forms stars approximately 20 million years prior to the *EarlyRe-apx*'s counterpart. Furthermore, throughout most of this halo's evolution, the stellar mass in *EarlyRe-ray* stays about several dex higher in the *EarlyRe-apx* version and relatively converge at the last snapshot. Thus, this shows that the choice of

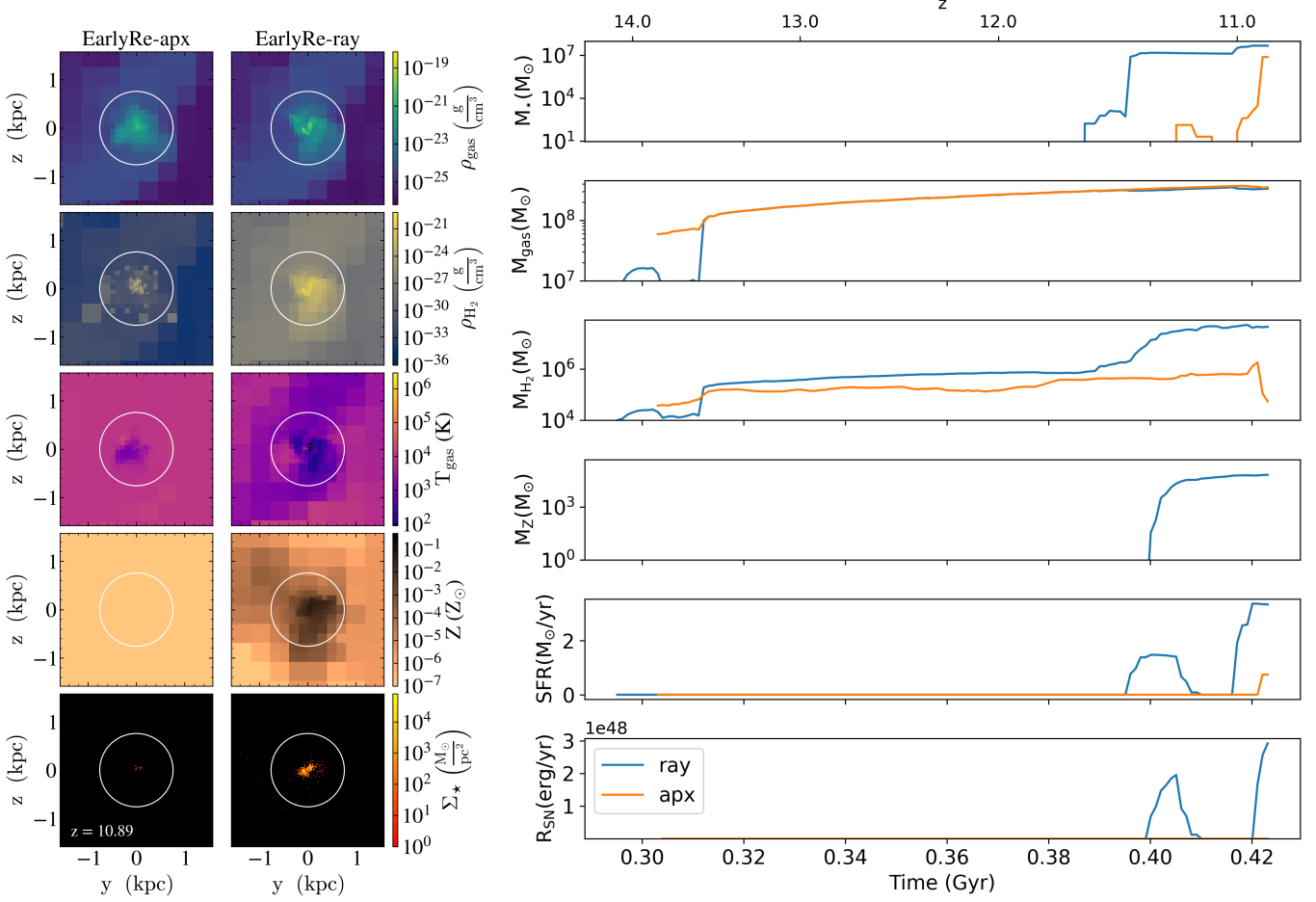


Figure 6. Same as Figure 5, but for another halo whose $M_{\text{halo}} \approx 1.7 \times 10^9 M_{\odot}$ at $z = 10.89$.

H₂ self-shielding model affects the timing of star formation in halos while the stellar mass between two models will eventually converge.

In addition to the difference in stellar mass, the star formation history shows that the halo in the ray-tracing model experience more prolonged period of star formation while the halo in the approximation model experience shorter but stronger star formation episode (**more detailed explanation maybe?**). This behavior also happens in other large halos in the simulation box (for brevity purpose, they are not shown in the paper). The prolonged star formation period leads to prolonged supernova rate, thus affecting the metal mixing and metal distribution of the galaxy. As supernovas go off in longer time period, more metals are produced at once and thus it takes a longer time for the metals to mixed with the surrounding gas. This leads to what we see in the metallicity projection plot, where metals are less mixed and more uniformly distributed in the *EarlyRe-ray* set. More metals also results in more efficient cooling

of gas, which is reflected in the temperature projection plot. These behaviors are more prominent in smaller halos, showing again that smaller halos are more susceptible by *H₂* self-shielding modeling than of bigger halos.

3.3. Effect on the galaxy and CGM

In this section, we more closely examine the effect of *H₂* self-shielding modeling on the ISM, the CGM, and the IGM to help further explain the previous observations we have on star formation.

Following the two case studies we examined in Section 3.2, Figures 7 and 8 show the gas and *H₂* phase plot of the largest halo in the simulation ($M_{\text{halo}} = 1.3 \times 10^{10} M_{\odot}$) and a smaller halo of mass $M_{\text{halo}} \approx 1.7 \times 10^9 M_{\odot}$. The plots are separated into the galaxy (top row) region and the CGM region (bottom row). One noticeable disparity between *EarlyRe-ray* and *EarlyRe-apx* is the inefficiency of the gas to cool down below $10^4 K$ due to the lack of molecular hydrogen in

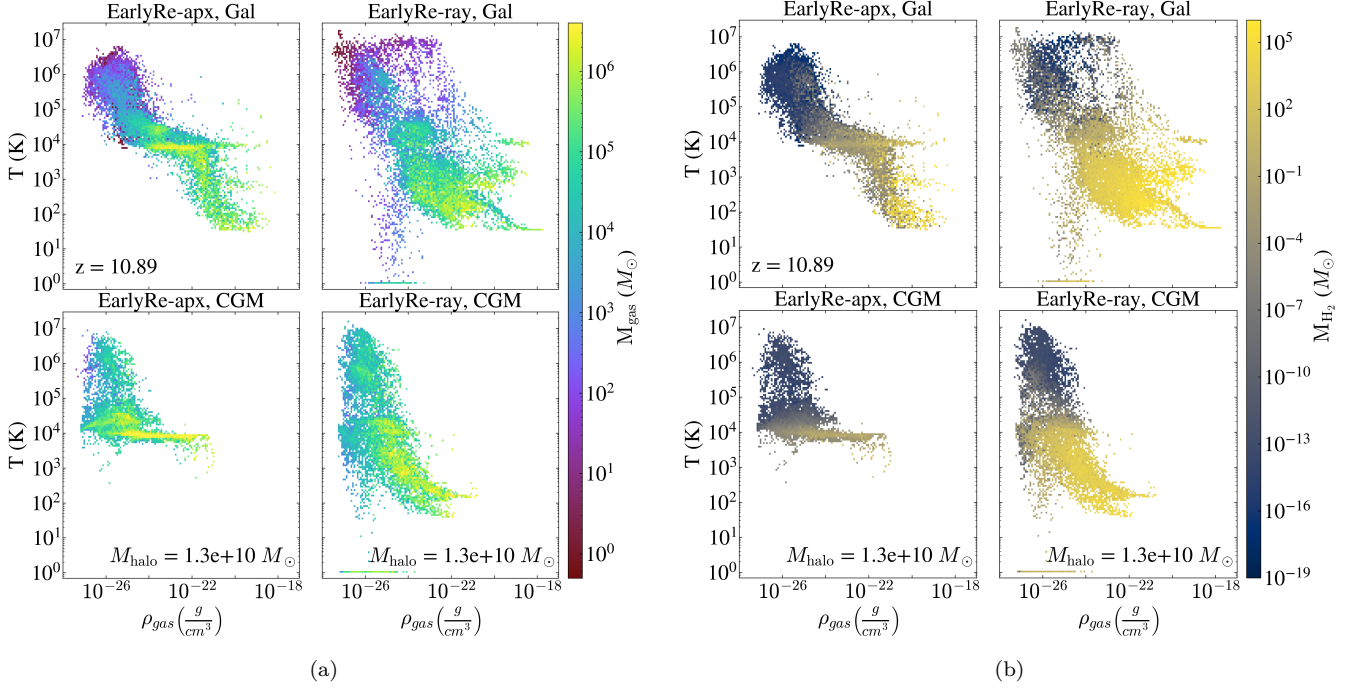


Figure 7. The gas phase plot colored by gas mass (Sub-figure (a)) and by molecular hydrogen mass (Sub-figure (b)) of the largest halo ($M_{\text{halo}} = 1.3 \times 10^{10} M_{\odot}$) in our simulation set, evaluated at the last time step $z = 10.89$. For each sub-figure, the left column shows the halo in *EarlyRe-apx*, and the right column shows its counterpart in *EarlyRe-ray*. The top row in each subfigure shows the phase plot using the gas cells within the galaxy region ($r \leq R_{\text{bary},2000}$), and the bottom row shows the phase plot using the gas cells in the CGM region ($R_{\text{bary},2000} < r \leq R_{\text{vir}}$).

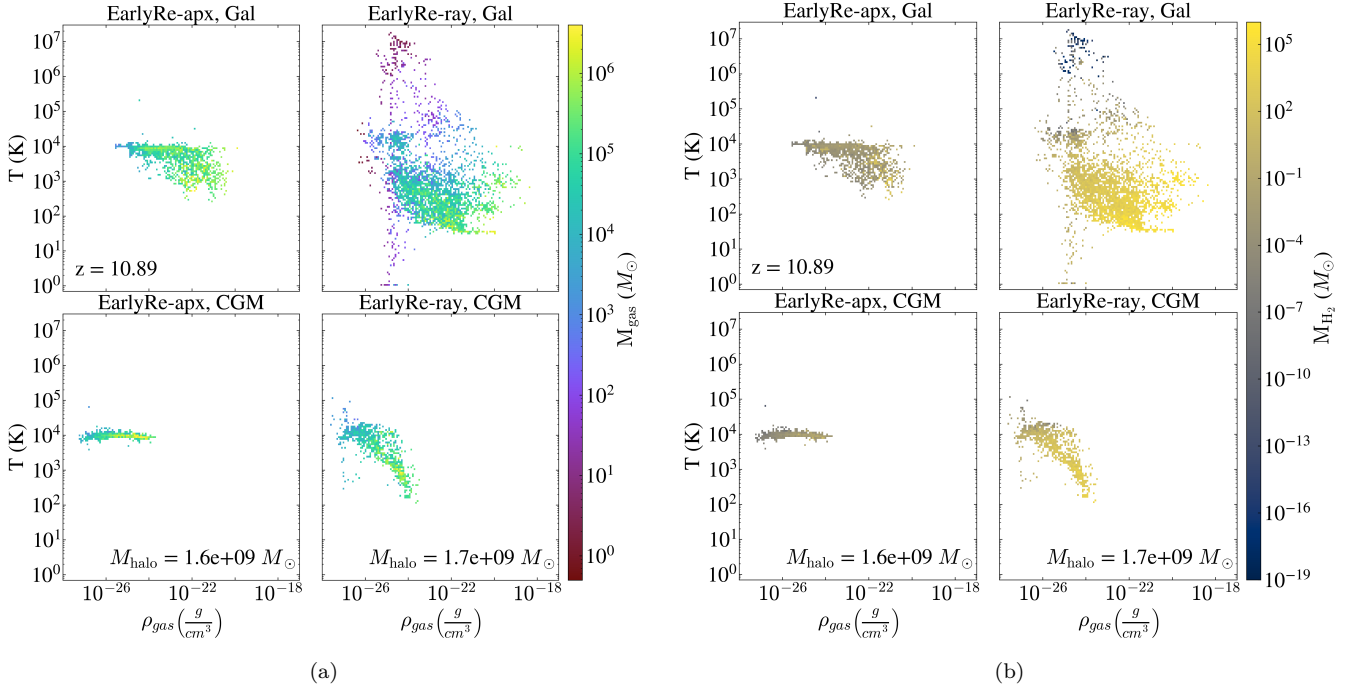


Figure 8. Similar to Figure 7, for a halo with $M_{\text{halo}} \approx 1.7 \times 10^9 M_{\odot}$ at $z = 10.89$.

the region. With atomic hydrogen HI being the only dominant component, processes such as Bremsstrahlung emission, atomic hydrogen's ionization and excitation processes can only help cool the gas down to $10^4 K$, while the existence of H_2 can introduce more energy levels to lower gas temperature. Thus, we can see a high concentration of gas at $10^4 K$ at low to intermediate density ($\rho_{\text{gas}} \leq 10^{-22} \text{ g/cm}^3$) when using the approximation model. The gas in *EarlyRe-apx* can only cool down to lower temperature after reaching a density of $\approx 10^{-22} \text{ g/cm}^3$ - the limit which the approximation model can better predict the H_2 self-shielding factor, according to Figure 1. When the gas is dense enough, the self-shielding of H_2 is approximated by *EarlyRe-apx* more accurately, leading to more H_2 to exist and gas to cool down. Indeed, according to the H_2 phase plot, H_2 exists most abundantly at the gas density of $\rho_{H_2} \geq 10^{-22} \text{ g/cm}^3$. The phase plot also re-affirm that the amount of H_2 existed in the *EarlyRe-apx*'s galaxy is much smaller than that of *EarlyRe-ray*, as pointed out in Figure 5. On the other hand, the large amount of molecular hydrogen in *EarlyRe-ray* existing even at low density helps cool down more of the gas. This allows gas to become denser. For example, the densest gas cell in the *EarlyRe-ray*'s galaxy in Figure 7 reaches the density above 10^{-18} g/cm^3 , about 10 to 100 times higher than the densest region in the *EarlyRe-apx*'s galaxy. It is important to note that for the radiative star cluster model and the Population III star model used in our simulation, their overdensity thresholds for a star particle to form are 10^7 and 10^6 , respectively. At the last time step ($z = 10.89$), these overdensity thresholds correspond to a gas density threshold of 4.5×10^{-20} and 4.5×10^{-21} . This suggests that both *EarlyRe-ray* and *EarlyRe-apx* galaxies are able to form stars; however, since *EarlyRe-ray* has more denser gas cells, it can form stars easier and quicker. **(so why the two stellar mass is the same?)** Furthermore, this effect is more prominent for lower halo. When using the approximation model, the gas within the *EarlyRe-apx*'s galaxy shown in Figure 8 cannot cool down below $10^3 K$ or gets denser than 10^{-20} g/cm^3 , while its counterpart can reach below $10^2 K$ and about 10^{-18} g/cm^3 thanks to much more H_2 being available.

In the CGM, gas has lower density and thus H_2 is more susceptible to destruction by LW radiation when using the approximation model. For both halos in our case studies, there is very little H_2 existing in the CGM in the *EarlyRe-apx* simulation. This keeps the gas in the CGM relatively hot at the minimum of $10^4 K$. In contrast, for *EarlyRe-ray* simulation, H_2 still exists in sufficient quantity outside of the galaxies that the CGM

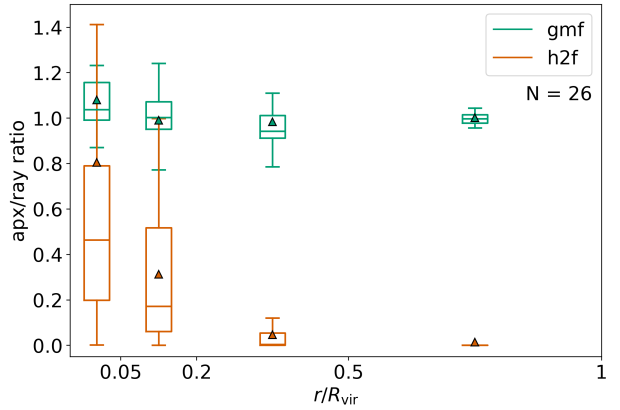


Figure 9. The comparison of the gas mass fraction (gmf) and H_2 fraction (h2f) in different radial bins (0 to $0.05 R_{\text{vir}}$, 0.05 to $0.2 R_{\text{vir}}$, 0.2 to $0.5 R_{\text{vir}}$, and 0.5 to $1 R_{\text{vir}}$) between the *EarlyRe-ray* and the *EarlyRe-apx* simulations at $z = 10.89$. The sample size for the statistics is 26 halos. The box represents the first and third quartile of the sample. The whiskers extend from the box to the further point within 1.5 times the inter-quartile range. The median is shown as a line in the box and the mean is shown as a triangle point.

gas can cool down to a few hundred kelvins. Therefore, the use of the self-shielding model significantly effect the temperature and density profiles of both the galaxy and the CGM.

The effect of the self-shielding model on different region of the halo is further illustrated in Figure 9, which shows the comparison between *EarlyRe-ray* and *EarlyRe-apx* with respect to the gas mass fraction and the H_2 fraction in four radial bins. We crossmatch and select halos whose gas is resolved enough for us to locate the baryonic center of mass and distinctly separate the halo into multiple bins. We end up with 26 halos, including halos without any stars, to calculate the statistics. The figure shows that while the gas mass fraction remains consistent between the two models across all radial bins, the ratio of H_2 fraction between the approximation and the ray tracing model shows a declining trend towards larger ratio. The H_2 fraction in *EarlyRe-apx* agrees with *EarlyRe-ray* only in the inner most region of the galaxy ($r < 0.05 R_{\text{vir}}$) where gas is at high density and thus the self-shielding factor is accurately calculated by the approximation model. As we go to the outer radius, gas density decreases and thus H_2 in *EarlyRe-apx* is under-shielded, leading to a decrease in the ratio of H_2 fraction. Further into the CGM ($r > 0.2 R_{\text{vir}} \approx R_{\text{bary},2000}$), the approximation model fails to estimate the self-shielding factor, leading to a clear absence of molecular hydrogen in this region when compared with the ray-tracing model.

It is important to note that we have an outlier in Figure 9 where a halo with mass $M_{\text{halo}} = 3.6 \times 10^{10} M_{\odot}$ has a H_2 fraction within $0.05R_{\text{vir}}$ about 8 times larger in *EarlyRe-apx* compared to *EarlyRe-ray*. To ensure the readability of the figure, we exclude this outlier from the figure; however, you can still see its effect on pulling the mean value away from the median value. The reason for this big difference is because for this particular halo, the gas in the inner region is much more compact and reaches a higher density in *EarlyRe-apx*. In particular, the densest gas cell in the *EarlyRe-apx*'s halo is about 10^{-19} g/cm^3 , 10 times higher than the *EarlyRe-ray*'s counterpart. At $\rho_{\text{gas}} \approx 10^{-19} \text{ g/cm}^3$, according to Figure 1, the Sobolev-like approximation typically overestimate the self-shielding amount, leading to more H_2 being able to form. More H_2 forming corresponds to more cooling, leading to the collapse of gas and increase in gas density. This results in a runaway effect that causes this halo to have noticeably high amount of H_2 in its inner region when using the approximation model. However, this halo is the only case where the H_2 fraction is considerably higher when using the approximation and it only happens near the galactic center. In most of the cases, this runaway effect only happens locally at a few dense gas cells (as also shown in the H_2 clumps in Figures 5 and 6) that it does not change the average H_2 fraction of the whole galactic region.

3.4. Effect on the large-scale universe and reionization

We extend our analysis to the whole simulation box to investigate the effect of H_2 self-shielding modeling on a large-scale universe. Figure 10 shows the projection plots at different snapshots within the simulation's refined region, which is about 1/10000 volume of the whole simulation box. While the large-scale structure of gas is similar between two simulations, the distribution of other properties differ greatly. The amount of molecular hydrogen in the ISM is much lower when using the Sobolev-like approximation method, especially after stars start to form in the simulation. Newly formed stars produce LW radiation that propagate the whole simulation's refined region and destroy H_2 in the low gas density region where the approximation model underpredicts the amount of shielding. The lowest H_2 density in the ISM of *EarlyRe-apx* is less than 10^{-36} g/cm^3 , while the H_2 density in the most diffuse region of *EarlyRe-ray* is nearly 10 dex higher. As the simulation progresses, H_2 is recreated surrounding the supernova's superbubbles and the galactic filaments. As we can see in the temperature projection plot, supernova explosions heat up and ionize the surrounding gas. The electron and proton created from the ionization provide ingredients

for H_2 to form (Galli & Palla 1998, see Table 1). However, near the supernova explosion when the temperature becomes too hot, H_2 can then be destroyed via collisional mechanism. These explains the accumulation of H_2 around galaxies and galactic filaments and the temporary absence of H_2 close to galaxies after stellar feedback in Figure 10. At high gas density region inside galaxies, H_2 can form via a three-body interaction between three atomic hydrogen (Palla et al. 1983) or via grain catalysis (Gould & Salpeter 1963).

As pointed out in Section 3.2, galaxies in *EarlyRe-ray* experience more prolonged star forming period than their counterparts in *EarlyRe-apx* and thus more metals are pushed out simultaneously in each period. This leaves shorter time for pristine gas to mix in to reduce the gas metallicity. Furthermore, more metals being produced at once helps contaminate the IGM more easily. When metals get out to the IGM, because of the medium's very low gas density for mixing, metallicity does not decrease over time, creating more extended metal-rich regions spanning out to the IGM in the ray-tracing simulation. It is important to note that this difference in metallicity originates from the difference in star formation history rather than the amount of metals being produced because the galaxies in two simulations have relatively similar stellar mass and total supernova energy, as shown in Figure 5.

As suggested by Figure 10, the universe in *EarlyRe-apx* is much hotter at $z \approx 10.9$ than its counterpart in *EarlyRe-ray*. Because cosmic reionization is linked to the heating of the IGM (D'Aloisio et al. 2019), we expect that reionization is affected by the choice of self-shielding modeling. Figure 11 shows the distribution of neutral hydrogen fraction χ_{HI} within the refined region between our two simulations. The χ_{HI} value of 0 corresponds to complete ionization of atomic hydrogen. High-energy radiation from galaxies ionizes hydrogen, decreasing χ_{HI} in the surrounding IGM regions. χ_{HI} can go up again during recombination between protons and electrons to form neutral hydrogen, which is efficient at temperature lower than 10^4 K (Wise 2019). In all time steps shown, *EarlyRe-apx* displays more extended and prominent region of ionized hydrogen, expanding out to the further IGM region. On the other hand, hydrogen is less ionized in *EarlyRe-ray*, and ionized hydrogen is limited around the galaxy filament (shown in the top two rows of Figure 10). This observation is quantified in Figure 12 where we plot the volume-weighted average of χ_{HI} within the simulation's refined region as a function of time. At the start of both simulations, the universe is dominated with neutral hydrogen ($\chi_{\text{HI}} \approx 1$). However, about 0.32 Gyr after the Big Bang ($z \approx 13.5$), the

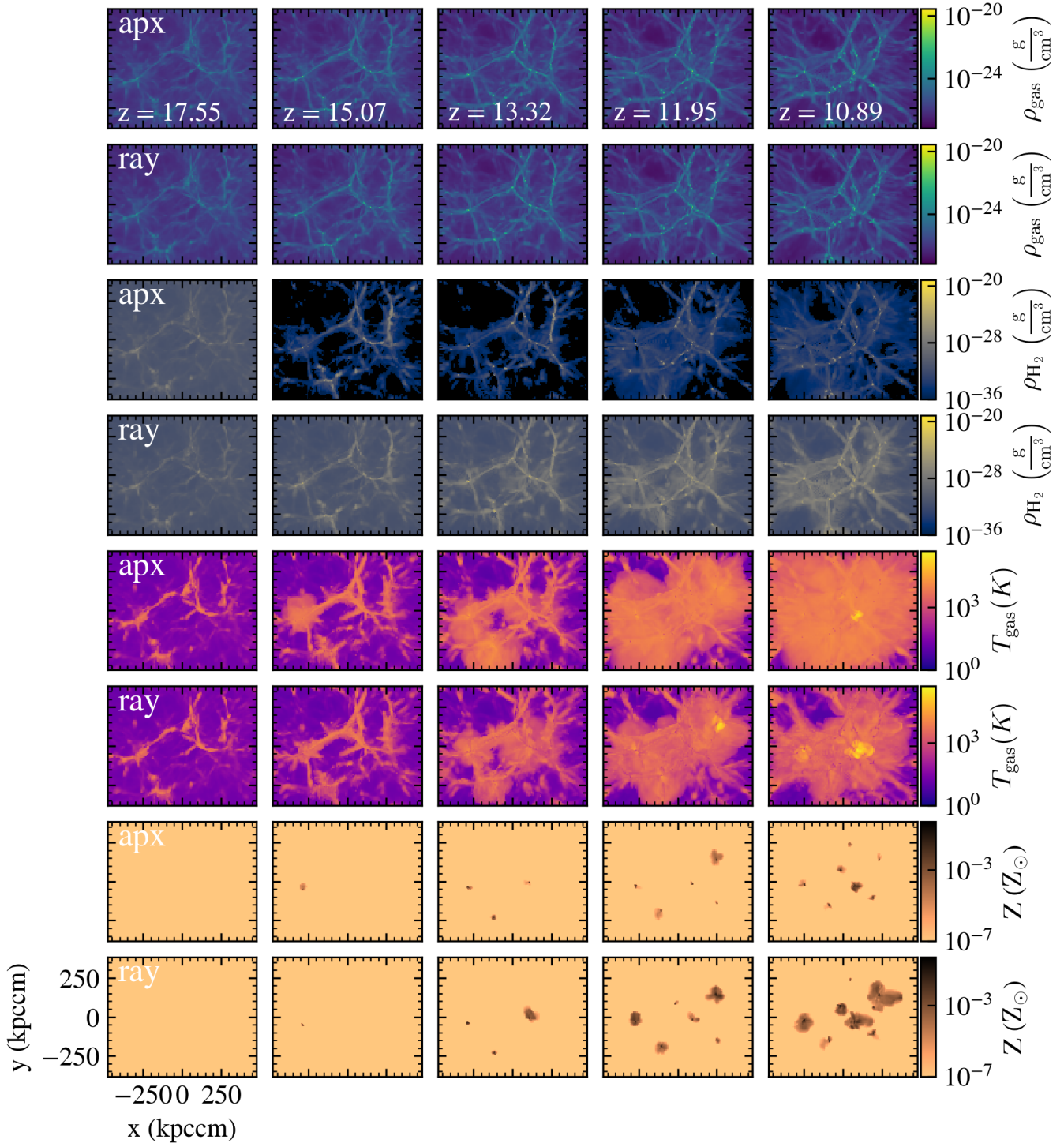


Figure 10. The gas density (1st and 2nd row), H_2 density (3rd and 4th row), gas temperature (5th and 6th row), and gas metallicity (7th and 8th row) within the simulation's refined region between the *EarlyRe-apx* and *EarlyRe-ray* across five time steps.

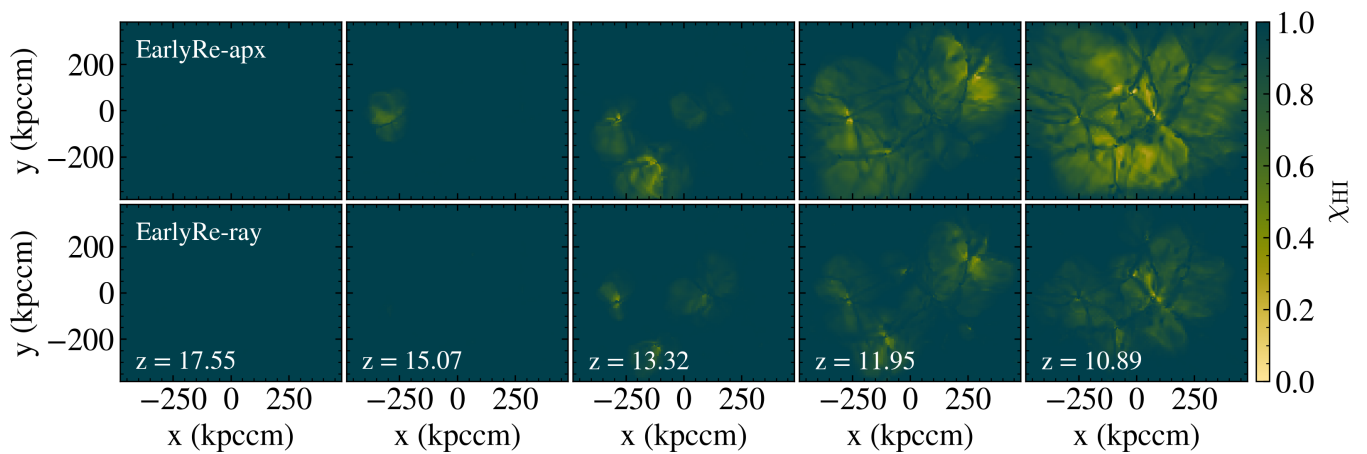


Figure 11. The neutral hydrogen fraction in the refined region box between the *EarlyRe-ray* and *EarlyRe-apx* simulations across five time steps.

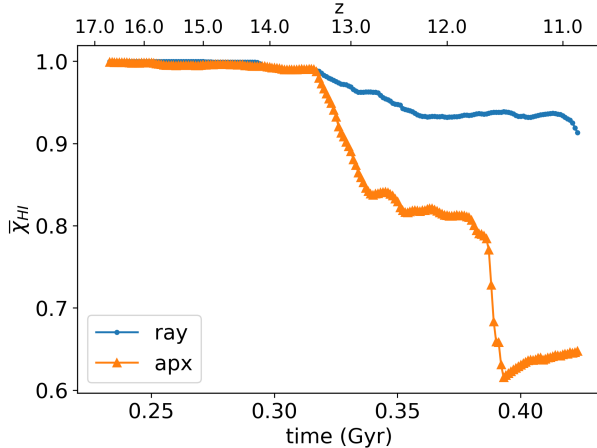


Figure 12. The comparison between the volume-weighted average of the neutral hydrogen fraction as a function of time between the *EarlyRe-ray* and the *EarlyRe-apx* simulations.

volume-weighted average of the neutral hydrogen fraction starts to drop considerably in the approximation model when the ray-tracing model only shows a slight decline. By the end of the simulation, while more than 90% of hydrogen is still neutral in *EarlyRe-ray*, only about 65% of hydrogen remains as such in *EarlyRe-apx*. While both simulations are not run long enough to cover the whole reionization epoch, Figure 12 suggests that the reionization may be complete earlier in *EarlyRe-apx* than in *EarlyRe-ray*, even though the reionization's start time is similar. This illustrates that the use of Sobolev-like approximation to model H_2 self-shielding speeds up the reionization process and thus affect our theoretical prediction and modeling of the reionization epoch.

4. DISCUSSION AND CONCLUSION

In this paper, using high-resolution zoom-in simulations, we run two radiative transfer models of molecular hydrogen self-shielding to examine their effect on galaxy evolution. The two models are the Sobolev-like approximation that uses local gas property to estimate the H_2 photodissociation rate and the ray tracing model based on HEALPix scheme. In summary, our key findings are as follows:

- The Sobolev-like approximation for H_2 self-shielding underestimates the self-shielding factor at low gas density ($\rho_{\text{gas}} \leq 10^{-22} \text{ g/cm}^3$) while overestimates the self-shielding factor at high gas density ($\rho_{\text{gas}} \geq 10^{-19} \text{ g/cm}^3$). This leads to halos in the simulation with the approximation model having their H_2 fraction several dex lower than their counterparts in the simulation with ray tracing model, especially for lower mass halo. (Figures 1 and 2)

The Sobolev-like approximation affects star formation in cosmological simulation. Lower-mass halos ($M_{\text{halo}} < 10^9 M_{\odot}$) are harder to form stars due to the lack of molecular hydrogen fuel. Bigger halos are less affected and still converge in stellar mass between the two models. (Figures 3, 4)

Even though there is convergence in the total stellar mass, the star formation history in the ray-tracing model shows more prolonged period of star formation while the approximation model shows a more bursty behavior. The different star formation behavior results in metals being produced, distributed, and mixed differently in the two simulation. This leads to a discrepancy in the metallicity and temperature profile between the two simulations where the ray-tracing model shows a more metal-riched and cooler ISM. (Figures 5, 6, and 10)

- Because the CGM is less dense than the galaxy, the effect of the approximation is more prominent in the outer region of the halo. Also, halos in the simulation with ray-tracing have more cool diffuse gas than in the simulation with the approximation model. (Figures 7, 8, and 9)
- The Sobolev-like approximation also effect the timing of the reionization epoch in cosmological simulation, where it make the universe reionize much quicker than the prediction using the ray tracing model. (Figures 11 and 12)

These results show that using the Sobolev-like approximation has a considerable impact on the prediction made with cosmological simulation, particularly with regards to H_2 , star formation activity in dwarf galaxies, and reionization period. For future work, we want to expand this comparison to other self-shielding approximation models as discussed in Section 1. It is possible that one method performs better in one aspect and worse in another, which makes it important for the simulation users to be aware and apply them accordingly to their scientific questions.

MORE DISCUSSION ON THE IMPACT AND FUTURE DIRECTION OF THE STUDY. ONE FUTURE DIRECTION IS TO DO THE COMPARISON FOR OTHER TYPES OF APPROXIMATION MODELS.

Acknowledgement: We would like to thank [insert Grant number] and CAPS fellowship.

REFERENCES

- 972 Abel, T., Wise, J. H., & Bryan, G. L. 2007, The
 973 Astrophysical Journal, 659, L87, doi: [10.1086/516820](https://doi.org/10.1086/516820)
- 974 Bryan, G. L., Norman, M. L., O'Shea, B. W., et al. 2014,
 975 The Astrophysical Journal Supplement Series, 211, 19,
 976 doi: [10.1088/0067-0049/211/2/19](https://doi.org/10.1088/0067-0049/211/2/19)
- 977 Chiaki, G., & Wise, J. H. 2023, Monthly Notices of the
 978 Royal Astronomical Society, 520, 5077,
 979 doi: [10.1093/mnras/stad433](https://doi.org/10.1093/mnras/stad433)
- 980 Christensen, C., Quinn, T., Governato, F., et al. 2012,
 981 Monthly Notices of the Royal Astronomical Society, 425,
 982 3058, doi: [10.1111/j.1365-2966.2012.21628.x](https://doi.org/10.1111/j.1365-2966.2012.21628.x)
- 983 D'Aloisio, A., McQuinn, M., Maupin, O., et al. 2019, The
 984 Astrophysical Journal, 874, 154,
 985 doi: [10.3847/1538-4357/ab0d83](https://doi.org/10.3847/1538-4357/ab0d83)
- 986 Davé, R. 2008, Monthly Notices of the Royal Astronomical
 987 Society, 385, 147, doi: [10.1111/j.1365-2966.2008.12866.x](https://doi.org/10.1111/j.1365-2966.2008.12866.x)
- 988 Draine, B. T., & Bertoldi, F. 1996, The Astrophysical
 989 Journal, 468, 269, doi: [10.1086/177689](https://doi.org/10.1086/177689)
- 990 Field, G. B., Somerville, R. B., & Dressler, K. 1966,
 991 Annual Review of Astronomy and Astrophysics, 4, 207,
 992 doi: [10.1146/annurev.aa.04.090166.001231](https://doi.org/10.1146/annurev.aa.04.090166.001231)
- 993 Galli, D., & Palla, F. 1998, Astronomy and Astrophysics,
 994 335, 403, doi: [10.48550/arXiv.astro-ph/9803315](https://doi.org/10.48550/arXiv.astro-ph/9803315)
- 995 Glover, S. C. O., & Mac Low, M.-M. 2007a, The
 996 Astrophysical Journal Supplement Series, 169, 239,
 997 doi: [10.1086/512238](https://doi.org/10.1086/512238)
- 998 —. 2007b, The Astrophysical Journal, 659, 1317,
 999 doi: [10.1086/512227](https://doi.org/10.1086/512227)
- 1000 Gnedin, N. Y., & Kravtsov, A. V. 2011, The Astrophysical
 1001 Journal, 728, 88, doi: [10.1088/0004-637X/728/2/88](https://doi.org/10.1088/0004-637X/728/2/88)
- 1002 Gnedin, N. Y., Tassis, K., & Kravtsov, A. V. 2009, The
 1003 Astrophysical Journal, 697, 55,
 1004 doi: [10.1088/0004-637X/697/1/55](https://doi.org/10.1088/0004-637X/697/1/55)
- 1005 Gorski, K. M., Hivon, E., Banday, A. J., et al. 2005, The
 1006 Astrophysical Journal, 622, 759, doi: [10.1086/427976](https://doi.org/10.1086/427976)
- 1007 Gould, R. J., & Salpeter, E. E. 1963, The Astrophysical
 1008 Journal, 138, 393, doi: [10.1086/147654](https://doi.org/10.1086/147654)
- 1009 Greif, T. H. 2014, Monthly Notices of the Royal
 1010 Astronomical Society, 444, 1566,
 1011 doi: [10.1093/mnras/stu1532](https://doi.org/10.1093/mnras/stu1532)
- 1012 Hartwig, T., Clark, P. C., Glover, S. C. O., Klessen, R. S.,
 1013 & Sasaki, M. 2015a, The Astrophysical Journal, 799, 114,
 1014 doi: [10.1088/0004-637X/799/2/114](https://doi.org/10.1088/0004-637X/799/2/114)
- 1015 Hartwig, T., Glover, S. C. O., Klessen, R. S., Latif, M. A.,
 1016 & Volonteri, M. 2015b, Monthly Notices of the Royal
 1017 Astronomical Society, 452, 1233,
 1018 doi: [10.1093/mnras/stv1368](https://doi.org/10.1093/mnras/stv1368)
- 1019 Johnson, J. L., Khochfar, S., Greif, T. H., & Durier, F.
 1020 2011, Monthly Notices of the Royal Astronomical Society,
 1021 410, 919, doi: [10.1111/j.1365-2966.2010.17491.x](https://doi.org/10.1111/j.1365-2966.2010.17491.x)
- 1022 Kannan, R., Macciò, A. V., Fontanot, F., et al. 2015,
 1023 Monthly Notices of the Royal Astronomical Society, 452,
 1024 4347, doi: [10.1093/mnras/stv1633](https://doi.org/10.1093/mnras/stv1633)
- 1025 Kennicutt, R. C. 1998, Annual Review of Astronomy &
 1026 Astrophysics, 36, 189,
 1027 doi: [10.1146/annurev.astro.36.1.189](https://doi.org/10.1146/annurev.astro.36.1.189)
- 1028 Kennicutt, R. C. J., Calzetti, D., Walter, F., et al. 2007,
 1029 The Astrophysical Journal, 671, 333, doi: [10.1086/522300](https://doi.org/10.1086/522300)
- 1030 Leroy, A. K., Walter, F., Sandstrom, K., et al. 2013, The
 1031 Astronomical Journal, 146, 19,
 1032 doi: [10.1088/0004-6256/146/2/19](https://doi.org/10.1088/0004-6256/146/2/19)
- 1033 Maio, U., Péroux, C., & Ciardi, B. 2022, Astronomy &
 1034 Astrophysics, 657, A47,
 1035 doi: [10.1051/0004-6361/202142264](https://doi.org/10.1051/0004-6361/202142264)
- 1036 O'Shea, B. W., Wise, J. H., Xu, H., & Norman, M. L. 2015,
 1037 The Astrophysical Journal, 807, L12,
 1038 doi: [10.1088/2041-8205/807/1/L12](https://doi.org/10.1088/2041-8205/807/1/L12)
- 1039 Palla, F., Salpeter, E. E., & Stahler, S. W. 1983, The
 1040 Astrophysical Journal, 271, 632, doi: [10.1086/161231](https://doi.org/10.1086/161231)
- 1041 Planck Collaboration, Ade, P. A. R., Aghanim, N., et al.
 1042 2016, Astronomy and Astrophysics, 594, A13,
 1043 doi: [10.1051/0004-6361/201525830](https://doi.org/10.1051/0004-6361/201525830)
- 1044 Safranek-Shrader, C., Krumholz, M. R., Kim, C.-G., et al.
 1045 2017, Monthly Notices of the Royal Astronomical Society,
 1046 465, 885, doi: [10.1093/mnras/stw2647](https://doi.org/10.1093/mnras/stw2647)
- 1047 Schmidt, M. 1959, The Astrophysical Journal, 129, 243,
 1048 doi: [10.1086/146614](https://doi.org/10.1086/146614)
- 1049 Shang, C., Bryan, G. L., & Haiman, Z. 2010, Monthly
 1050 Notices of the Royal Astronomical Society, 402, 1249,
 1051 doi: [10.1111/j.1365-2966.2009.15960.x](https://doi.org/10.1111/j.1365-2966.2009.15960.x)
- 1052 Sobolev, V. V. 1957, Soviet Astronomy, 1, 678
- 1053 Stecher, T. P., & Williams, D. A. 1967, The Astrophysical
 1054 Journal, 149, L29, doi: [10.1086/180047](https://doi.org/10.1086/180047)
- 1055 Stevens, A. R. H., Martig, M., Croton, D. J., & Feng, Y.
 1056 2014, Monthly Notices of the Royal Astronomical Society,
 1057 445, 239, doi: [10.1093/mnras/stu1724](https://doi.org/10.1093/mnras/stu1724)
- 1058 Thoul, A. A., & Weinberg, D. H. 1995, The Astrophysical
 1059 Journal, 442, 480, doi: [10.1086/175455](https://doi.org/10.1086/175455)
- 1060 Wise, J. H. 2019, Contemporary Physics, 60, 145,
 1061 doi: [10.1080/00107514.2019.1631548](https://doi.org/10.1080/00107514.2019.1631548)
- 1062 Wise, J. H., & Abel, T. 2011, Monthly Notices of the Royal
 1063 Astronomical Society, 414, 3458,
 1064 doi: [10.1111/j.1365-2966.2011.18646.x](https://doi.org/10.1111/j.1365-2966.2011.18646.x)
- 1065 Wise, J. H., & Cen, R. 2009, The Astrophysical Journal,
 1066 693, 984, doi: [10.1088/0004-637X/693/1/984](https://doi.org/10.1088/0004-637X/693/1/984)

- ¹⁰⁶⁷ Wolcott-Green, J., Haiman, Z., & Bryan, G. L. 2011,
¹⁰⁶⁸ Monthly Notices of the Royal Astronomical Society, 418,
¹⁰⁶⁹ 838, doi: [10.1111/j.1365-2966.2011.19538.x](https://doi.org/10.1111/j.1365-2966.2011.19538.x)
- ¹⁰⁷⁰ Wong, T., & Blitz, L. 2002, The Astrophysical Journal,
¹⁰⁷¹ 569, 157, doi: [10.1086/339287](https://doi.org/10.1086/339287)
- ¹⁰⁷² Yoshida, N., Abel, T., Hernquist, L., & Sugiyama, N. 2003,
¹⁰⁷³ The Astrophysical Journal, 592, 645, doi: [10.1086/375810](https://doi.org/10.1086/375810)
- ¹⁰⁷⁴ Yoshida, N., Oh, S. P., Kitayama, T., & Hernquist, L. 2007,
¹⁰⁷⁵ The Astrophysical Journal, 663, 687, doi: [10.1086/518227](https://doi.org/10.1086/518227)
- ¹⁰⁷⁶ Yoshida, N., Omukai, K., Hernquist, L., & Abel, T. 2006,
¹⁰⁷⁷ The Astrophysical Journal, 652, 6, doi: [10.1086/507978](https://doi.org/10.1086/507978)